Bidirectional Switchable Metalens Based on Phase Change Materials of GST

Yuke Li, Yuxuan Chen, Zexu Liu, Yipan Lou, Yi Lian, Chang Jiang, Jicheng Wang ⬥, and Xianqin Li

Abstract—**Metalens can achieve more challenging functions especially dynamic regulation than traditional lens due to its unprecedented ability to manipulate light. In this paper, an approach to realizing switchable bidirectional metalens is proposed based on phase change material GST. Two geometric parameters of nanopillars were designed to demonstrate full phase modulation due to the Pancharatnam-Berry phase. According to the phase distribution, we realize the flexible control of the metalens through the transition of states. These special designs of unit structures make multi-focal point focus and two-dimensional focus also realized. In addition, the bidirectional switchable metalens have been realized through the transformation of states on a bilayer metasurface substrate. Its unique phase transition properties which are not available to previous metasurface can be applied in high quality imaging cameras, optical microscopes, lidar scanning systems, etc.**

Index Terms—**Metasurface, phase change materials, multidimensional focus.**

I. INTRODUCTION

METASURFACE, as the promising 2D equivalents of metamaterial [1], has been widely concerned and applied to manipulate the phase, amplitude and polarization due to its excellent performance. At present, many planar optical components have been implemented, including metalens [2], [3], [4], [5], vortex-beam generators [6], [7] holographic image [8], [9] and coding metasurface [10], [11], [12]. In terms of regulation principle, the traditional optical element regulates light through the phase delay in the cumulative propagation process, which makes it difficult to miniaturize and integrate devices. The optical field regulation of the metasurface is mainly based on Huygens-Fresnel principle. This principle states that, the local response of each meta-structure surface element to incident light can be regarded as a secondary wave source, the optical field regulation is accomplished by optimizing the parameters and

The authors are with the Jiangnan University, Wuxi 214122, China (e-mail: 2954971830@qq.com; 853470185@qq.com; 3267911775@qq.com; 1051947615@qq.com; 2876581306@qq.com; 3395146956@qq.com; jcwang@jiangnan.edu.cn; 825911077@qq.com).

spatial ordering of the metasurface unit. In particular, the dynamic switchable metasurface can further extend the application range of the metasurface, widen the working band or realize the switching of different functions of optical devices [13]. Dynamic modulated metasurface can currently be implemented in three ways: First, we can adjust the angle wavelength or polarization state of the incident light directly [14]. The other method is to reversibly change the geometric parameters of the metasurface by combining micro-electro-mechanical System (MEMS), femtosecond laser overwriting, stretchable substrate [15] etc. The third one is using various methods such as phase change materials (PCM) [16], temperature, electric and magnetic fields [17], and chemical reactions to adjust the refractive index and related parameters. Low-loss optical PCMs have enabled new optical performance, with superb characteristics to realize switchable, high-saturation, high-efficiency and high-resolution dynamic meta-pixels [18]. Some particular phase change material (PCM) can be easily repeated between crystalline and amorphous state. Especially, electrically tunable phase change metasurface is an important platform [19] and chalcogenide PCMs have excellent performance [20]. Ge2Sb2Te5 (GST) is an outstanding phase-change material which can be excited by temperature [21], light [22] and electricity [23]. The choice between crystalline and amorphous states exhibits dramatic difference in optical and electrical characteristics [24]. Its refractive index changes greatly in the infrared band allowing for simulation using the refractive index model [25]. For example, Zhang et al. produced tunable wave plates based on GST metasurface [26], while Dong et al. discussed the tunable filter in mid-infrared band [27]. Guo et al. also realized the switchable multi-angle beam deflection and multi-focus in the mid-infrared band by using GST metasurface [28]. Additionally, Xu et al. realized achromatic lenses with large operation bandwidth using bilayer architecture. However, most of the metasurface functions can only be realized on one side and the functional structure is relatively simple [29].

In this paper, we propose the bidirectional metalens based on phase change material GST to broaden the application range of metasurface. We designed two geometric parameters of nanopillars to demonstrate the full phase modulation under circularly polarized light. According to the phase distribution, the flexible control of the metalens was realized through the transition of states as a switch. The unexpected modulation ability of unit structure makes multi-focal point focus and two-dimensional focus also realized. Bidirectional switchable metalens have been realized based on a thick substrate to avoid the interference of
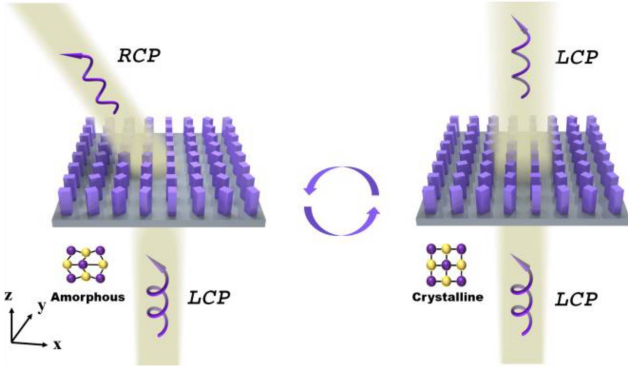
Fig. 1. Schematic diagram of beam deflection of phase transition metasurface during crystalline and amorphous transitions based on GST. When the circularly polarized light is incident, it is deflected in the amorphous state.

Fig. 2. (a)–(b) Schematic diagram of the "A" unit cell; (d)–(e) schematic diagram of the "B" unit cell; (c)–(f) the transmission spectra of the "A" and "B" unit cells respectively in the different states.

two sides. The novel research has provided a reference for high quality imaging cameras, optical microscopes, lidar scanning systems, etc.

II. MODEL DESIGN AND THEORIES

In this research, the working wavelength was chosen as 2500 nm because of its low absorption loss in this wavelength. It is feasible to change the operating wavelength to other mid-infrared bands by adjusting the geometric parameters of the GST nanopillars since the loss of GST in the mid-infrared band is still low [30]. This provides a good prospect for biomedical, military, mechanical and other fields. There are many intermediate states between the crystalline and amorphous states, which can be characterized by the dielectric constant. Lorentz-Lorentz relation is adopted to describe GST under different crystallinity [16]:

$$\frac{\varepsilon_{\text{eff}}(\lambda) - 1}{\varepsilon_{\text{eff}}(\lambda) + 2} = m \frac{\varepsilon_{\text{cGST}}(\lambda) - 1}{\varepsilon_{\text{cGST}}(\lambda) + 2} + (1 - m) \frac{\varepsilon_{\text{aGST}}(\lambda) - 1}{\varepsilon_{\text{aGST}}(\lambda) + 2} \quad (1)$$

Where $\varepsilon_{cGST}(\lambda)$ and $\varepsilon_{aGST}(\lambda)$ are the functions of GST permittivity to wavelength in crystalline state and amorphous state respectively, m represents the GST crystallization fraction, whose value ranges from 0 to 1.

The phase-change metasurface is composed of GST square column and glass substrate, as shown in Fig. 1. The outstanding phase change metasurface can generate different optical effects due to the flexibility and adjustability of GST without changing incident light and geometric parameters. Fig. 1 shows when the GST is completely in amorphous state (m = 0), incident a left-handed circularly polarized light (LCP) from below, the transmitted light is converted to right-handed circularly polarized (RCP) light and the transmitted light will be deflected in one direction. As the crystallinity changes from 0 to 1, the Angle of deflection changes gradually. Until GST is completely transformed to the crystalline state (m = 1), the polarization and direction of the transmitted light remain the same as that of the incident light. We will discuss the state when $m = 1$ and $m = 0$, while other states can be adjusted accordingly.

Fig. 2(a) shows the unit cell of the "A" nanopillars, which are periodic along x and y directions. We used the physics simulation
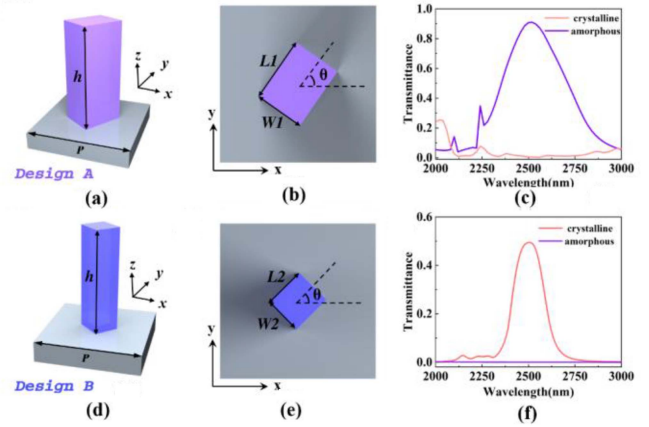
software COMSOL to optimize the parameters to obtain reasonable structural dimensions. We set periodic boundary conditions for the x and y directions of the structure and set a perfect matching layer in the z direction. In order to reduce the loss, we use SiO_2 as the substrate. We set the substrate thickness to 200 nm, and its refractive index is 1.4298 in 2500 nm. The length, width and height are respectively chosen as 505, 388, 1200 nm ($L_1 = 505$ nm, $W_1 = 0.77L_1$, $h = P = 1200$ nm). The incident light is incident vertically from the bottom. Fig. 2(b) presents the transmission spectra of the "A" nanopillar, we found that the GST in the crystalline state has nearly no transmittance, but in amorphous state there is a transmission peak up to 0.91 in 2500 nm wavelength. We also designed another structure in Fig. 2(c) called "B" nanopillars. Its length is changed to 272 nm, and the width is 0.9 times of the length ($L_2 = 272$ nm, $W_2 = 0.9L_2$). The height is the same as "A" nanopillars. Fig. 2(d) shows the transmission spectra of the "B" nanopillar, GST in crystalline state has imaginary part so that its transmission peak is lower than "A" nanopillar.

Based on the above discussion, the design of GST nanopillars plays a crucial role in achieving the desired tunability of the metasurface. By controlling the shape, size, and orientation of each nanopillar, a metasurface can perform different functions by manipulating wavefronts on a sub-wavelength scale. In particular, the phase control is the focus of this paper. The phase response of nanostructures can be designed by many methods, including resonant phase, geometric phase, and propagation phase. We prefer to use the geometric phase, which is also called Pancharatnam-Berry phase (P-B phase). This control mode does not require changing the structural parameters; it can be achieved simply by rotating the angle of the structure. This requires us to design cuboid pillars and utilize the P-B phase to design the response of nanopillars.

To realize a high-efficiency metalens, we further design the phase of the transmitted light based on the geometric parameters of the two nanopillars that have been optimized. Based on geometric parameters theory [12], the main effect on the phase is circularly polarized light. When a circularly polarized light
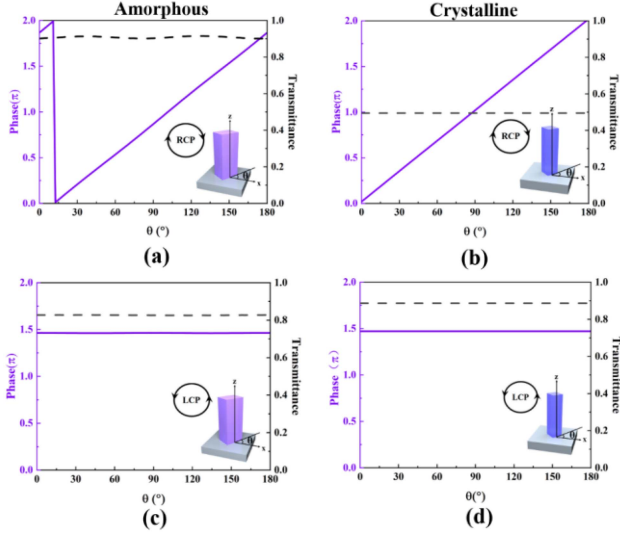
Fig. 3. (a)–(c) The change of transmittance and phase of right-handed circularly polarized (RCP) and left-handed circularly polarized (LCP) transmitted light respectively with rotation angle detected when left-handed circularly polarized (LCP) incident light for "A" nanopillars in the amorphous state; (b)–(d) the change of transmittance and phase of right-handed circularly polarized (RCP) and left-handed circularly polarized (LCP) transmitted light respectively with rotation angle detected when left-handed circularly polarized (LCP) incident light for "B" nanopillars in the crystalline state.

Fig. 4. The switching of focus demonstrated by the array of two nanopillars ("A" and "B"); (a), (b) electric field distribution and normalized intensity curves (z = 20 μm) of "A" nanocrystalline array in crystalline and amorphous states; (c), (d) electric field distribution and normalized intensity curves (z = 25 μm) of "B" nanocrystalline array in crystalline and amorphous states.

incident on the metasurface, the co-polarization component of the transmitted light is the same as that of the incident light and is independent of the rotation angle (θ) of nanopillars. The other component, called the cross-polarization component, is opposite to the polarization of the incident light and has an extra phase. The spin state of the incident light is $\sigma = \pm 1$, which respectively represents left-handed circularly polarized (LCP) light and right-handed circularly polarized (RCP) light. As shown in Fig. 3(a), we calculate the relation between the transmittance and phase of right-handed circularly polarized (RCP) light in the transmitted light and the rotation angle (θ) of the "A" nanopillars when using left-handed circularly polarized (LCP) light as the incident light. The calculation results are that the phase has a linear relationship with θ, which can be covered in the range of 0~2π. While the transmittance does not change with the change of θ, and basically stays at 0.9. In Fig. 3(b), when the "A" nanopillars are converted to a crystalline state, the transmitted light is left-handed circularly polarized (LCP), and the phase does not change with θ.

On the other hand, we also do the same research in "B". Fig. 3(c) shows the phase of "B" nanopillars can also be linearly changed from 0 to 2π by rotating the angle of nanopillars. The transmittance also does not vary with θ and remains around 0.5. Similarly, the transmittance and phase of the left-handed circularly polarized transmitted light is regulated by "B" do not change with θ in Fig. 3(d). Based on the above discussion, we can control the phase by changing the rotation angle (θ) of the nanopillars while maintaining high transmittance. This provides a good condition for the following design of metalens.
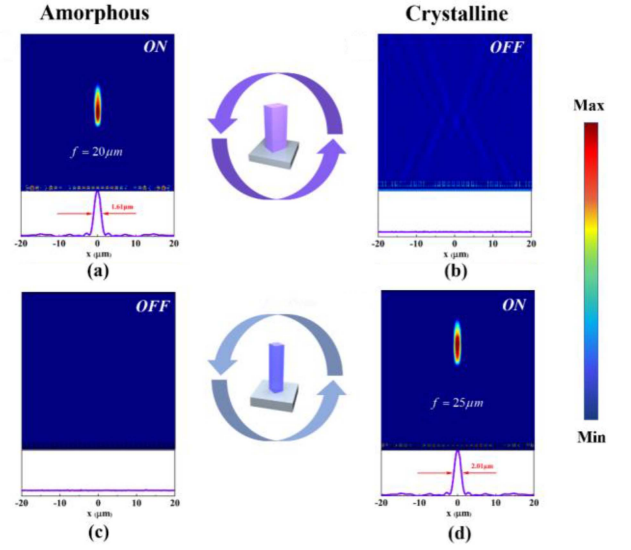
III. RECONFIGURABLE FOCUS METALENS WITH CONTROLLABLE SWITCH

According to the above phase regulation, we can design switchable focus state. We have designed two types of unit cells that can be used to perform two different functions. According to the principle of Pancharatnam-Berry phase, its simple control mode makes the reconfiguration easy to achieve. In order to realize the function of metalens, we need phase gradient array. Then, for the focus of a two-dimensional light field, the phase can be expressed as:

$$\varphi (x - x_0) = -\frac{2\pi}{\lambda} \left(\sqrt{(x - x_0)^2 + f^2} - |f| \right) - 2n\pi \quad (2)$$

where λ represents the operating wavelength of the incident source, f is the focal length, x is the position of every unit cell and the x_0 is the focal position. The last additional term is used to limit the value of the phase in 0~2π. According to (2), we adjust the rotation angles of two nanopillars A and B, and arranged 33 unit cells to achieve the effect. We designed two focal lengths ($f_1 = 20$ μm, $f_2 = 25$ μm) based on A and B nanopillars respectively. The numerical aperture is expressed as:

$$NA = \sin \left[\tan^{-1} \left(\frac{D}{2f} \right) \right] \quad (3)$$

where D is the array diameter. The numerical aperture of the two lenses can be calculated as: $NA_1 = 0.7035$, $NA_2 = 0.6209$. The results obtained from the simulation are shown in Fig. 4, metalens exhibits excellent focusing properties, and the focal point is located at the expected position. Fig. 4(a) illustrates the modulation effect of A nanopillars. When "A" nanopillars are in the amorphous state, the focusing effect is realized in 20 μm. But when it is converted to the crystalline state, the focusing effect

disappears, are depicted in Fig. 4(b). In Fig. 4(c) and (d), the modulation effect of B nanopillars is in the reverse: the focusing effect is realized in 25 μm in the crystalline state and disappeared in the amorphous state. We also introduce the depth of focus (DOF) to show the quality of focus, which is measured by the full width at half maximum (FWHM). As shown in Fig. 4(a) and (d), the normalized intensity of the x-transversal at the focal point can be regarded as pulsing response. The DOF values are calculated as 1.61 μm and 2.01 μm and indicate the quality of the focus points is excellent.

IV. ONE-DIMENSIONAL MULTI-FOCAL METALENS

In certain applications, multi-focus lenses are introduced to distribute the energy of an incident plane wave in different regions of the focal plane [31], [32], [33]. In this section, we respectively design the transverse and longitudinal multi-focus modes to broaden the application range of the metalens. According to the amplitude distribution theory, horizontal double focusing is assumed, the distance between the two focal points is $2d$. The distance between the two focal points and the metasurface is respectively $r_1 = (f_1^2+(d+x)^2)^{1/2}$ and $r_2 = (f_2^2+(d-x)^2)^{1/2}$. Thus, The equation of plane wave superposition at reference point $(x, 0)$ can be expressed as:

$$\vec{E} = \vec{E}_1 + \vec{E}_2 = \frac{1}{r_1}\exp\left(\vec{j}\vec{k}_1\right)\hat{e}_1 + \frac{1}{r_2}\exp\left(\vec{j}\vec{k}r_2\right)\hat{e}_2 \quad (4)$$

The phase change of light refraction can be expressed as:

$$\tan\varphi(x) = \frac{(1/r_1)\sin kr_1 + (1/r_2)\sin kr_2}{(1/r_1)\cos kr_1 + (1/r_2)\cos kr_2} \quad (5)$$

The array phase distribution on the metasurface can still be based on (2). In the lateral focusing mode, the phase distribution can be represented as follows:

$$\varphi(x - x_0) =$$

$$\begin{cases} 2\pi/\lambda\left(\sqrt{(x-x_0)^2 + f_1^2}-|f_1|\right)-2n\pi & -D/2 \le x < 0 \\ 2\pi/\lambda\left(\sqrt{(x-x_0)^2 + f_2^2}-|f_2|\right)-2n\pi & 0 < x \le D/2 \end{cases}$$

$$(6)$$

where D is the total width of the array f_1 and f_2 are the focal lengths of the two focal points respectively. The results are shown in Fig. 5(a). Two focal points are located in (-20 μm, 25 μm) and (20 μm,25 μm). It can be observed that the two focal points exhibit minimal interference with each other, thereby meeting the expected requirements. We also calculate the full width at half maximum (FWHM) and light intensity in Fig. 5(b). There is a pulse peak at -20 μm and 20 μm with a half-height width of 1.94 μm and 2.00 μm, respectively. This means that the metalens still maintained excellent focus performance in multi-focus mode.

Analogously, the longitudinal double focusing can also be achieved, similar to the horizontal double focus. The distance from any point on the metasurface becomes $r_1 = (f_1^2+x^2)^{1/2}$ and $r_2 = (f_2^2+x^2)^{1/2}$. The equation of plane wave superposition and the phase change of light refraction are the
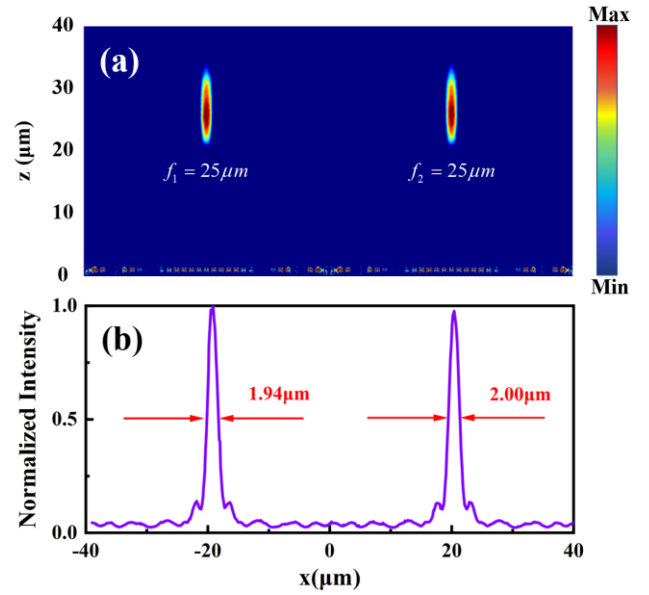

Fig. 5. (a) Horizontal double focus distribution, focus positions are (-20 μm, 25 μm) and (20 μm, 25 μm). (b) The normalized intensity of two focus points. The full widths at half maximum (FWHM) are 1.94 μm and 2.00 μm.
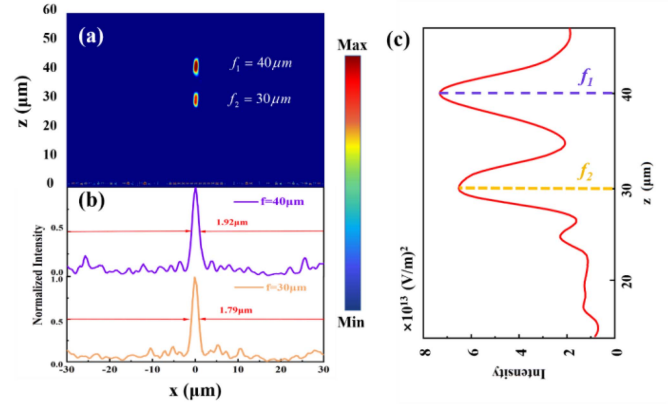

Fig. 6. (a) Electric field distribution of longitudinal double-focus, focus positions are (0, 30 μm) and (0, 40 μm) respectively; (b) the normalized intensity curves of two focus points in z = 30 μm and z = 40 μm; (c) the intensity curve at x = 0.

same as the horizontal double focus. The simulation results are shown in Fig. 6. Fig. 6(a) shows the simulated electric field results, and the two focal points are respectively at (0, 30 μm) and (0, 40 μm), which is consistent with the theoretical results. In Fig. 6(b), the normalized intensity is calculated at two focal points respectively, again with excellent quality. The full widths at half maximum (FWHM) are 1.79 μm and 1.92 μm respectively. What's more, we calculate the z-axis intensity when $x = 0$ in Fig. 6(c).

V. TWO-DIMENSIONAL FOCAL METALENS

We have discussed the many different applications of metalens in one dimensional focus. However, achieving one-dimensional focus is difficult in practical applications. In this section we
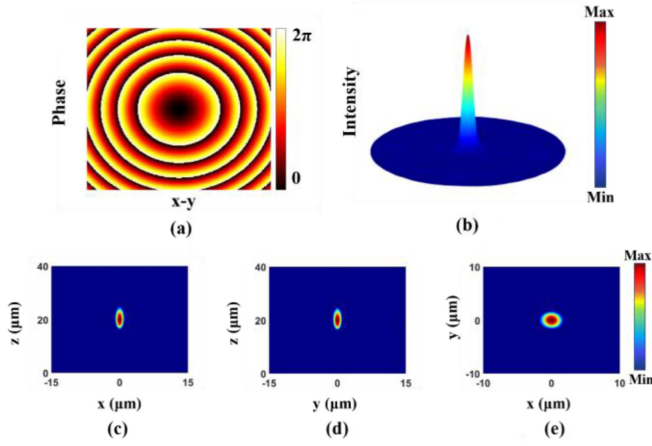
Fig. 7. (a) Phase profile of the 30 × 30 array in the x-y plane; (b) the height expression of the square of the field mode intensity at the focal point in the x-y plane; (c)–(e) the intensity distributions on the x-z, y-z, and x-y planes respectively at the focal point f = 20 μm.

propose a two-dimensional focus to suit practical application. For two-dimensional focus, the phase distribution of the array can be expressed as:

$$\varphi(x,y) = 2\pi/\lambda \left(\sqrt{R^2 + f^2} - |f| \right) - 2n\pi \qquad (7)$$

where $R = (x^2+y^2)^{1/2}$ is the distance from any point to the origin on the 2D plane. Due to the complexity of the two-dimensional array, we use the finite-Difference Time-domain (FDTD) software of Lumerical to solve the simulation. Using this software combined with MATLAB, the array can be arranged by code, which greatly reduces the workload.

In order to more accurately verify the focusing ability of the metalens, we design a 30 × 30 array. According to the (7), the phase distribution in the *x-y* plane can be obtained as shown in Fig. 7(a). The array is arranged according to the phase distribution, we set the focus at (0, 0, 20 μm). The simulation results are shown in Fig. 7(c)–(e). We have plotted the intensity distributions on the *x-z*, *y-z*, and *x-y* planes. In the *x-z* and *y-z* faces plane, the focus point is at 20 μm. The focus exhibits very good quality compared to the one-dimensional array. The full width at half maximum (FWHM) has been calculated to be 1.40 μm both in *x-z* and *y-z* plane. In the *x-y* plane, it can be clearly seen that the focal spot has a circularly symmetric shape and the cross-section exhibits an Airy disk distribution with a radius of 1.40 μm. We also calculate the height expression of the intensity at the focal point in the *x-y* plane in Fig. 7(b). It is clear that there is a strong impulse response at the focal point and the surrounding sidelobe is almost negligible. Through the above analysis, we demonstrate the excellent lensing quality of the designed two-dimensional metalens.

VI. BIDIRECTIONAL SWITCHABLE FOCAL METALENS

In the above discussion, we design two kinds of metalens unit structure, "A" and "B", and realized phase control of amorphous state and crystalline state respectively. In this section, to nanopillars arrays are arranged on both sides of a thick SiO2 substrate
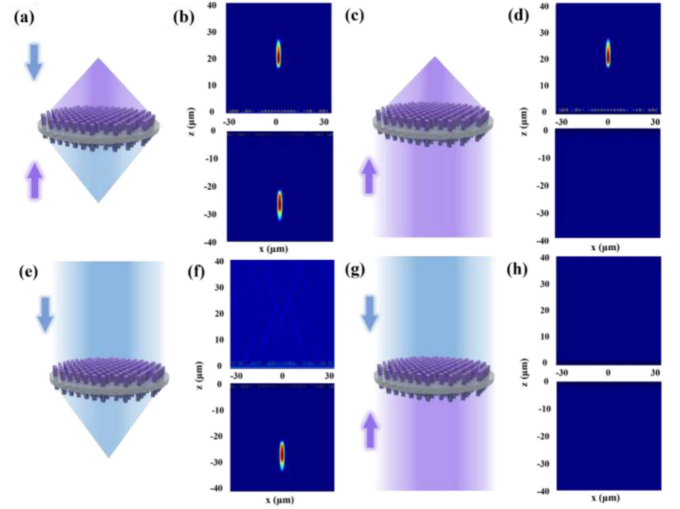

Fig. 8. (a), (b) Schematic diagram and electric field distribution of bidirectional focusing (the upper layer "A" is amorphous, and the lower layer "B" is crystalline); (c), (d) schematic diagram and electric field distribution of upper layer focusing (both upper and lower layers are amorphous); (e), (f) schematic diagram and electric field distribution of lower layer focusing (both upper and lower layers are crystalline); (g), (h) schematic diagram and electric field distribution of focus disappears (upper layer "A" is crystalline, and the lower layer "B" is amorphous).

to realize bidirectional phase regulation. To meet fabrication limitations and eliminate crosstalk between the two layers of the optical field modulation units, the dielectric thickness between them is usually set to be larger than multiple incident wavelengths, and it is always greater than the Talbot length. The Talbot length is defined as $\lambda_T = 2P^2/\lambda$, and in this study, the Talbot length is 1.152 μm, which should be smaller than the chosen gap distance. The typical value for eliminating near-field crosstalk is twice the wavelength length [34], [35]. Thus, we set the thickness of substrate as 5 μm. The upper layer of the bidirectional metasurface consists of an "A" nanopillars array and the lower layer of a "B" nanopillars array. In order to reduce the sidelobe of focus and improve the imaging quality, we adopt a circular array arrangement.

Fig. 8(a) shows that when voltage is applied to the "A" nanopillars in the upper layer, the upper layer changes into an amorphous state while the "B" nanocrystal nanopillars in the lower layer remain in a crystalline state. When incident light is incident from above and below at the same time, bidirectional focus can be realized. As shown in Fig. 8(b), the focus of the upper layer is 20 μm by the regulation of "A" nanopillars, and the focus of the lower layer is 25 μm by the regulation of "B" nanopillars. When both structures are amorphous and incident light is only incident from the bottom, the upper layer produces A focus of 20 μm regulated by the "A" nanopillars are shown in Fig. 8(c) and (d). However, when both structures are in a crystalline state and the incident light is only incident from the top, the lower layer generates a focus of 25 μm regulated by the "B" nanopillars. However, when the upper part changes to a crystal state and the lower part to the amorphous state, no matter how the incident light source, there is no exact effect. This shuts down the function of the metalens in essence. Therefore, by

changing the state of GST, the metalens can realize four different functions. There is no need to change the parameters of the structure in this process, and it is even possible to simply rotate the angle of the column to get the focus of different positions.

VII. CONCLUSION

In summary, we combine analytical calculations and modern numerical simulations to design and evaluate an array of two-layer structures. The designed structures achieve the transmittance of up to 0.91 in the amorphous state and can satisfy the phase regulation of $0 \sim 2\pi$. By adjusting the crystallization fraction of the GST, we achieved flexible control of the metalens according to the designed phase. The unexpected modulation ability of unit structure makes multi-focal point focus and two-dimensional focus also realized. Bidirectional switchable metalens have been demonstrated based on a thick substrate to avoid the interference from two sides. The ultrathin design of metalens can extend the applications, strictly subject to space limitations, in various technological fields especially high-quality imaging cameras and optical microscopes.

REFERENCES

[1] N. Yu et al., "Light propagation with phase discontinuities: Generalized laws of reflection and refraction," *Science*, vol. 334, no. 6054, pp. 333–337, Oct. 2011.

[2] M. Li, M. Liu, Y. Chen, Z.-D. Hu, J. Wu, and J. Wang, "All-dielectric metasurface lenses for achromatic imaging applications," *Nanoscale Res. Lett.*, vol. 17, no. 1, Sep. 2022, Art. no. 81.

[3] F. Aieta et al., "Aberration-free ultrathin flat lenses and axicons at telecom wavelengths based on plasmonic metasurfaces," *Nano Lett.*, vol. 12, no. 9, pp. 4932–4936, Sep. 2012.

[4] C. Chen et al., "Parallel polarization illumination with a multifocal axicon metalens for improved polarization imaging," *Nano Lett.*, vol. 20, no. 7, pp. 5428–5434, Jul. 2020.

[5] C. Xia et al., "A polarization-insensitive infrared broadband achromatic metalens consisting of all-silicon anisotropic microstructures," *Appl. Phys. Lett.*, vol. 121, no. 16, Oct. 2022, Art. no. 161701.

[6] B. Zhang, Z. Hu, J. Wang, J. Wu, and S. Tian, "Creating perfect composite vortex beams with a single all-dielectric geometric metasurface," *Opt. Exp.*, vol. 30, no. 22, Oct. 2022, Art. no. 40231.

[7] K. Cheng, Z. Liu, Z.-D. Hu, G. Cao, J. Wu, and J. Wang, "Generation of integer and fractional perfect vortex beams using all-dielectric geometrical phase metasurfaces," *Appl. Phys. Lett.*, vol. 120, no. 20, May 2022, Art. no. 201701.

[8] L. Huang et al., "Three-dimensional optical holography using a plasmonic metasurface," *Nature Commun.*, vol. 4, no. 1, Nov. 2013, Art. no. 2808.

[9] Q. Song et al., "Ptychography retrieval of fully polarized holograms from geometric-phase metasurfaces," *Nature Commun.*, vol. 11, no. 1, May 2020, Art. no. 2651.

[10] X. Huang, Z. Liu, Y. Lian, Z.-D. Hu, J. Wu, and J. Wang, "Dynamic beam all-direlectric coding metasurface converter based on phase change materials of GST," *Opt. Laser Technol.*, vol. 159, Apr. 2023, Art. no. 109037.

[11] M. Ma et al., "Optical information multiplexing with nonlinear coding metasurfaces," *Laser Photon. Rev.*, vol. 13, no. 7, Jul. 2019, Art. no. 1900045.

[12] S. Liu et al., "Convolution operations on coding metasurface to reach flexible and continuous controls of terahertz beams," *Adv. Sci.*, vol. 3, no. 10, Oct. 2016, Art. no. 1600156.

[13] T. Badloe, J. Lee, J. Seong, and J. Rho, "Tunable metasurfaces: The path to fully active nanophotonics," *Adv. Photon. Res.*, vol. 2, no. 9, Sep. 2021, Art. no. 2000205.

[14] S. M. Kamali, E. Arbabi, A. Arbabi, Y. Horie, M. Faraji-Dana, and A. Faraon, "Angle-multiplexed metasurfaces: Encoding independent wavefronts in a single metasurface under different illumination angles," *Phys. Rev. X*, vol. 7, no. 4, Dec. 2017, Art. no. 041056.

[15] Z. Wang et al., "Thermally reconfigurable hologram fabricated by spatially modulated femtosecond pulses on a heat-shrinkable shape memory polymer for holographic multiplexing," *ACS Appl. Mater. Interfaces*, vol. 13, no. 43, pp. 51736–51745, Nov. 2021.

[16] J. Tian et al., "Active control of anapole states by structuring the phase-change alloy Ge2Sb2Te5," *Nature Commun.*, vol. 10, no. 1, Jan. 2019, Art. no. 396.

[17] K. Guo et al., "Tunable oriented mid-infrared wave based on metasurface with phase change material of GST," *Results Phys.*, vol. 34, Mar. 2022, Art. no. 105269.

[18] O. Hemmatyar et al., "Enhanced meta-displays using advanced phase-change materials," Jul. 2021, *arXiv:2107.12159*.

[19] S. Abdollahramezani et al., "Electrically driven reprogrammable phase-change metasurface reaching 80% efficiency," *Nature Commun.*, vol. 13, no. 1, Mar. 2022, Art. no. 1696.

[20] "Tunable nanophotonics enabled by chalcogenide phase-change materials," Accessed: Jun. 16, 2023. [Online]. Available: https://www.degruyter.com/document/doi/10.1515/nanoph-2020-0039/html

[21] K.-K. Du et al., "Control over emissivity of zero-static-power thermal emitters based on phase-changing material GST," *Light Sci. Appl.*, vol. 6, no. 1, Jul. 2016, Art. no. e16194.

[22] Q. Wang et al., "Optically reconfigurable metasurfaces and photonic devices based on phase change materials," *Nature Photon.*, vol. 10, no. 1, pp. 60–65, Jan. 2016.

[23] P. Hosseini, C. D. Wright, and H. Bhaskaran, "An optoelectronic framework enabled by low-dimensional phase-change films," *Nature*, vol. 511, no. 7508, pp. 206–211, Jul. 2014.

[24] M. Khorasaninejad, W. T. Chen, R. C. Devlin, J. Oh, A. Y. Zhu, and F. Capasso, "Metalenses at visible wavelengths: Diffraction-limited focusing and subwavelength resolution imaging," *Science*, vol. 352, no. 6290, pp. 1190–1194, Jun. 2016.

[25] K. Shportko, S. Kremers, M. Woda, D. Lencer, J. Robertson, and M. Wuttig, "Resonant bonding in crystalline phase-change materials," *Nature Mater.*, vol. 7, no. 8, pp. 653–658, Aug. 2008.

[26] D.-Q. Zhang, F.-Z. Shu, Z.-W. Jiao, and H.-W. Wu, "Tunable wave plates based on phase-change metasurfaces," *Opt. Exp.*, vol. 29, no. 5, Mar. 2021, Art. no. 7494.

[27] W. Dong et al., "Tunable mid-infrared phase-change metasurface," *Adv. Opt. Mater.*, vol. 6, no. 14, Jul. 2018, Art. no. 1701346.

[28] K. Guo et al., "Tunable oriented mid-infrared wave based on metasurface with phase change material of GST," *Results Phys.*, vol. 34, Mar. 2022, Art. no. 105269.

[29] Y. Wang, Q. Fan, and T. Xu, "Design of high efficiency achromatic metalens with large operation bandwidth using bilayer architecture," *Opto-Electron. Adv.*, vol. 4, no. 1, 2021, Art. no. 200008.

[30] L. T. Chew et al., "Chalcogenide active photonics," *Proc. SPIE*, vol. 10345, pp. 58–66, 2017.

[31] X. Zang et al., "A multi-foci metalens with polarization-rotated focal points," *Laser Photon. Rev.*, vol. 13, no. 12, Dec. 2019, Art. no. 1900182.

[32] H. Pang, H. Gao, Q. Deng, S. Yin, Q. Qiu, and C. Du, "Multi-focus plasmonic lens design based on holography," *Opt. Exp.*, vol. 21, no. 16, Aug. 2013, Art. no. 18689.

[33] L. Zhu et al., "Polarization-controlled tunable multi-focal plasmonic lens," *Plasmonics*, vol. 12, no. 1, pp. 33–38, Feb. 2017.

[34] S. Wang et al., "Broadband achromatic optical metasurface devices," *Nature Commun.*, vol. 8, Aug. 2017, Art. no. 187.

[35] X. Che et al., "Generalized phase profile design method for tunable devices using bilayer metasurfaces," *Opt. Exp.*, vol. 29, no. 26, Dec. 2021, Art. no. 44214.